High antinoise photoacoustic tomography based on a modified filtered backprojection algorithm with combination wavelet

Lvming Zeng, Da Xing,[a)] Huaimin Gu, Diwu Yang, Sihua Yang, and Liangzhong Xiang
MOE Key Laboratory of Laser Life Science & Institute of Laser Life Science, South China Normal University, Guangzhou 510631, People's Republic of China

How to extract the weak photoacoustic signals from the collected signals with high noise is the key to photoacoustic signal processing. We have developed a modified filtered backprojection algorithm based on combination wavelet for high antinoise photoacoustic tomography. A *Q*–switched-Nd: yttrium–aluminum–garnet laser operating at 532 nm is used as light source. The laser has a pulse width of 7 ns and a repetition frequency of 20 Hz. A needle polyvinylidene fluoride hydrophone with diameter of 1 mm is used to capture photoacoustic signals. The modified algorithm is successfully applied to imaging vascular network of a chick embryo chorioallantoic membrane *in situ* and brain structure of a rat brain *in vivo*, respectively. In the reconstructed images, almost all of the capillary vessels and the vascular ramifications of the chick embryo chorioallantoic membrane are accurately resolved, and the detailed brain structures of the rat brain organization are clearly identified with the skull and scalp intact. The experimental results demonstrate that the modified algorithm has much higher antinoise capacity, and can greatly improve the reconstruction image quality. The spatial resolution of the reconstructed images can reach 204 μm. The modified filtered backprojection algorithm based on the combination wavelet has the potential in the practical high-noise signal processing for deeply penetrating photoacoustic tomography. © *2007 American Association of Physicists in Medicine*. [DOI: 10.1118/1.2426406]

Key words: photoacoustic tomography, combination wavelet, antinoise capacity, noise, filtered backprojection

I. INTRODUCTION

Photoacoustic tomography (PAT) combines the advantages of both pure optical imaging and pure ultrasound imaging, which can provide high ultrasonic resolution and high optical contrast tissue images.[1–5] The basic idea of PAT is that a tissue is irradiated with nanosecond laser pulses, the deposited energy may result in a thermo-elastic expansion and subsequent contraction of the irradiated volume that generates time-trace photoacoustic waves, which can be detected by high sensitive transducers around the tissue. The strength and the profile of the captured photoacoustic signals carry the spatial information of the light absorption distribution of the tissue, which is often related to its character of structure, physiological and pathological changes, because tissues in different physiology conditions have different light absorption coefficients.[6,7] For example, the absorption contrast between breast tumors and normal breast tissues can be as high as 500% at the near infrared;[8] the absorption contrast between the blood and the surrounding medium is around 1000% for 850 nm light.[9]

In order to extract the weak photoacoustic signals, a focused transducer with big aperture may give us a good signal-to-noise ratio (SNR), because the SNR is proportional to the square root of the aperture area, and then the measured data are used to construct an image directly. However, the focal diameter and length of the transducer limit the lateral resolution and the image view, respectively.[10] An alternative method is to use an unfocused transducer with small aperture

to detect photoacoustic signal and then reconstruct the absorption distribution based on a special algorithm. The different measurement configuration may result in a different reconstruction algorithm. Examples of approximate reconstruction methods include the multi-element phase-controlled technique,[11] the deconvolution algorithm,[12] the weighted delay-and-sum method,[13] the optimal statistical approach,[14] and the Radon transform in far-field approximation.[15] Exact reconstruction algorithms are recently derived for various detection geometries.[16–19] Filtered backprojection (FBP) method based on rotation scanning configuration is a classical algorithm to reconstruct the cross-sectional image. The quality of reconstructed image is mainly determined by choosing different filters, such as Ramachandran and Lakshminarayanan (RL), Shepp and Logan (SL), Modi-SL and Kwoh-Reed, etc. Virtually, Gibbs phenomena appearing in the filter's response may bring a mass of image blurring. Moreover, the noise suppression of the classical FBP algorithm is unsatisfied. With an increased detecting depth, the background white noise of photoacoustic signals increases rapidly and changes into strong nonwhite noise after backprojection, leading to a serious deterioration of imaging quality, which drastically restricts the applicable depth of PAT in the medical field to a great extent. Therefore, it has great practical significance to find a new filter method with better filtering precision and noise suppression.

In recent years, wavelet transform combining the best features of time and frequency methods (e.g., Fourier transform
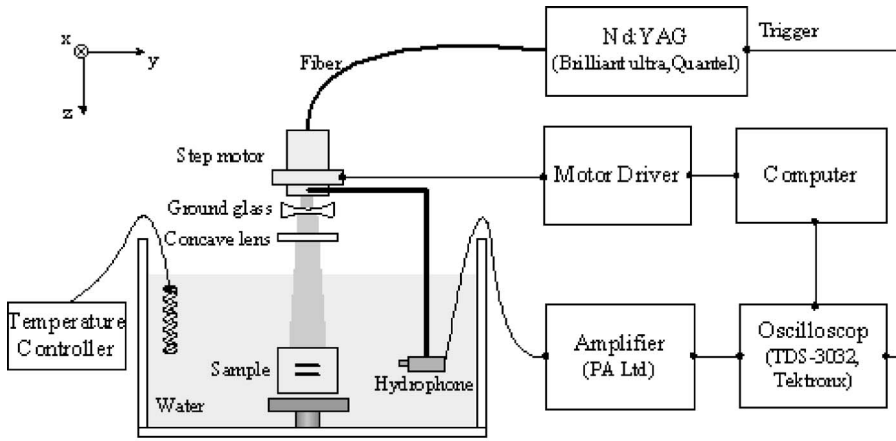
FIG. 1. Schematic experimental setup for PAT imaging.

methods) is rapidly becoming a new approach for antinoise signal processing[20,21] and biomedical image reconstruction.[22–24] In this paper, we develop a modified FBP (mFBP) algorithm based on combination wavelet for high-noise PAT. The results indicate that the wavelet-based mFBP algorithm effectively improves the resolution and contrast of reconstruction images on the condition of strong background noise, which can potentially be developed as a high antinoise photoacoustic reconstruction technique to diagnose deeply embedded tumors.

II. MATERIALS AND METHODS

A. Imaging system

A schematic experimental setup for PAT is shown in Fig. 1, where a laboratory coordinate system $[X, Y, Z]$ is also depicted. A Q-switched Nd: yttrium–aluminum–garnet laser is employed as the pumping source operates at 532 nm with pulse width of 7 ns and repetition frequency of 20 Hz. The laser beam is expanded by a concave lens and homogenized by a ground glass and then onto the sample from above along the Z axis. The incident laser energy density on the sample surface is controlled below $\sim$20 mJ/cm^2, which is the maximum permissible exposure for skin to a laser beam at a wavelength of 532 nm. The distribution of optical absorption of the test sample generated proportionate photoacoustic waves, which are coupled into a needle polyvinylidene fluoride hydrophone (Precision Acoustics Ltd.) with a diameter of 1 mm and a sensitivity of 950 nv/pa. The signals accepted from the hydrophone are subsequently amplified by a pre-amplifier, then recorded by a digital oscilloscope (TDS3032, Tektronix), and finally transferred to a personal computer for further data processing using MATLAB (ver 7.0, Mathworks). The hydrophone is driven by a step motor to scan around the sample along a 96-mm-diam circle in the X-Y plane. The sample and hydrophone are both immersed in a tank of water for coupling the photoacoustic waves to the hydrophone. The induced photoacoustic waves are captured every 1.8°, and total 200 positions are recorded for a full view of 2π circular scanning angle. The sampling rate of the oscilloscope in our experiment is 250 MS/s. The experimental setup has some improvement compared with our previous system published in PMB paper (2004).[12] For example, changing to rotate the transducer for animal sample and capturing signals on more positions. In the experiments, a temperature controller is used to keep the body temperature of the intravital sample through thermal transmittance of the coupling medium, and the speed of sound is kept relatively constant at 1500 m/s.

B. Imaging principle

Wavelet analysis is breaking up of a signal into shifted and scaled versions of the original wavelet. Suppose that an analytic wavelet function $\Psi(t)$ is subject to the conditions as follows:

$$\Psi(t) \in L^1(R,dt) \cap L^2(R,dt) \tag{1}$$

and

$$\hat{\Psi}(\omega) \in L^1\left[R \setminus \{0\}, \frac{d\omega}{|\omega|}\right] \cap L^2\left[R \setminus \{0\}, \frac{d\omega}{|\omega|}\right], \tag{2}$$

where $L^1(R)$ and $L^2(R)$ denote two function spaces which can be absolute integrable and square integrable, respectively; $\hat{\Psi}(\omega)$ is the Fourier transform of the wavelet function $\Psi(t)$, and $\hat{\Psi}(\omega)=0$ when $\omega<0$. Consider an arbitrary function $f(t) \in L^2(R,dt)$, whose wavelet transform of the original wavelet function $\Psi(t)$ is defined as

$$W_f(b,a) = \frac{1}{a}\int_{-\infty}^{+\infty} f(t)\bar{\Psi}\left[\frac{t-b}{a}\right]dt. \tag{3}$$

Then the following theorem can be deduced:[25]

$$\frac{1}{C_\Psi}\int_0^{+\infty} W_f(b,a)\frac{da}{a} = f(b) + iH[f(b)], \tag{4}$$

under the admissible condition,

$$C_\Psi = \int_0^{+\infty} \frac{\hat{\Psi}_R(\omega)}{\omega}d\omega < \infty, C_\Psi \neq 0, \tag{5}$$

where $\bar{\Psi}(t)$ is the conjugate function of $\Psi(t)$; $\hat{\Psi}_R(\omega)$ is the real part of $\hat{\Psi}(\omega)$; $H[f(b)]$ is the Hilbert transform of $f(t)$.

Because of the finite bandwidth of an ultrasound transducer, the projections of optical absorption distribution can be reconstructed using the FBP algorithm,[12]

$$\oiint_{|r|=ct} A(r)ds = \frac{4\pi C_p kt}{\beta r_p} \cdot IFFT\left(\frac{P_{dt}(\omega)W(\omega)}{P_{d0}(\omega)}\right), \quad (6)$$

where the $W(\omega)$ filter is the key to the reconstructed photoacoustic image quality. Theoretically, the reconstructed algorithm based on inverse Radon transform needs the $W(\omega)$ filter to be equal to $|\omega|$, which is an ideal Hilbert filter gene with an infinite bandwidth. However, according to Paley-Wiener theorem, it cannot be realized in practice. Moreover, the classical filter may bring strong Gibbs phenomena and has a bad antinoise capacity, so the quality of reconstructed image is dissatisfied. The induced photoacoustic pressures $P_r(t)$ can be obtained directly by deconvolving the recorded photoacoustic signal $P_{d0}(t)$ originating from a point absorption source with the fast inverse Fourier transform,

$$P_r(t) = IFFT\left(\frac{P_{dt}(\omega)}{P_{d0}(\omega)}\right), \quad (7)$$

so we can rewrite Eq. (6) as

$$\oiint_{|r|=ct} A(r)ds = \frac{4\pi C_p kt}{\beta r_p} \cdot IFFT\left(\frac{P_{dt}(\omega)}{P_{d0}(\omega)}\right) * IFFT[W(\omega)]$$

$$= \frac{4\pi C_p kt}{\beta r_p} \cdot P_r(t) * \left(-\frac{1}{2\pi^2 t^2}\right), \quad t \neq 0$$

$$= \frac{2 C_p kt}{\beta r_p} \cdot \left[\frac{\partial}{\partial t} P_r(t)\right] * \left(\frac{1}{\pi t}\right)$$

$$= \frac{2 C_p kt}{\beta r_p} \cdot H\left[\frac{\partial}{\partial t} P_r(t)\right] \quad (8)$$

by setting

$$f(t) = \frac{\partial}{\partial t} P_r(t). \quad (9)$$

Then, according to the theorem in Eq. (4), finally we get

$$\oiint_{|r|=ct} A(r)ds = \frac{2\pi C_p kt}{\beta r_p} \cdot \text{Im}\left[\frac{1}{C_\Psi} \int_0^{+\infty} F_p(t,a)\frac{da}{a}\right], \quad (10)$$

where

$$F_p(b,a) = -\frac{1}{a^2} \int_{-\infty}^{+\infty} P_r(t) \cdot \Psi'\left(\frac{t-b}{a}\right)dt, \quad (11)$$

$\Psi'(t)$ is the differential of the wavelet function $\Psi(t)$ and "*" denotes convolution. From the upward formulas, it can be seen that the convolution operation of projected data can be substituted by wavelet transform. A frequency spectrum of the photoacoustic signal has a major section from a few megahertz to tens of megahertz, for example, blood vessel sizes of about $100-300$ μm are most sensitive to the transducer with a central frequency between 4.5 and 10 MHz.[2] However, a single wavelet transform is impracticable to execute signal band processing, so a combination of multiple wavelets (combination wavelet) is used to realize wide bandpass processing. We choose a modified Morlet wavelet as the mother wavelet, and then the combination wavelet can be obtained as follows:

$$g(t) = \Psi_m(t)\sum_{k=1}^{n} \exp[2\pi j(f_L - f_m + k\Delta f)t],$$

$$(k = 0, 1, \ldots, n), \quad (12)$$

where

$$\Psi_m(t) = [\cos mt + i\sin mt] \cdot \exp\left[-\frac{1}{2}\left(\frac{\sqrt{2}\sigma m}{2\pi\tau}t\right)^2\right]$$

$$+ \text{correction term}, \quad (13)$$

$g(t)$ is the combination wavelet; $\Psi_m(t)$ is the mother wavelet; f_m is the central frequency of $\Psi_m(t)$; f_L is the lower limiting frequency of $g(t)$; Δf is the spacing of the central frequency of the combined wavelets, so the upper limiting frequency of $g(t)$ is $f_H = f_L - f_m + n\Delta f$. The correction term can be ignored when $[\pi\tau/\sqrt{2}\sigma]^2$ is great enough.[25] Although the laser-induced ultrasonic waves range widely in the frequency spectrum, a single ultrasonic transducer can only respond to part of the spectrum because of its limited bandwidth. The extreme values of f_L and f_H are determined by the bandwidth of the ultrasound transducer. The higher frequency spectral range provided better image resolution while the lower frequency spectral range delineated the major structural traits. Therefore, choosing the value of f_L and f_H should weigh imaging resolution and sensitivity. The value of Δf affects the frequency spectral superposition effect of combined wavelets, and the suitable value of σ (the Gauss parameter of mother wavelet) makes the form of the chosen wavelet basis functions similar to the PAT signal. In this paper, the main parameters have the following appropriate properties: $f_L = 200$ KHz, $f_H = 15$ MHz, $\Delta f = 200$, $\sigma = 0.2$, $\tau = 4$, $m = 6$.

To decompose the measured data with wavelet method, the energy distribution of the true signal can be concentrated within space Swb on the condition that the form of the chosen wavelet basis function is similar to the true signal. So the others outside of the space Swb could be seen as the primarily noise data, whose coefficients will be relatively small compared to that of the true signal. Comparable noise reduction could be accomplished by reconstructing the image through standard methods, decomposing the image into a complete set of wavelet basis functions, and then zeroing out all components of the image that are outside of the space Swb spanned by a restricted set of wavelets, which has a good character of wide bandpass filter to extract the interested information. The wavelet coefficients are kept or zeroed according to a number of thresholds, which are defined by the so-called SURE thresholding technique. It follows that noise could be reduced, without greatly reducing the signal, by restricting the processed data to the space Swb. If the noise or the interference wave appears in some frequency or time slice of the space Swb, adding some preprocessing to the frequency or time slice could reduce the image distortion in terms of suppression noise.
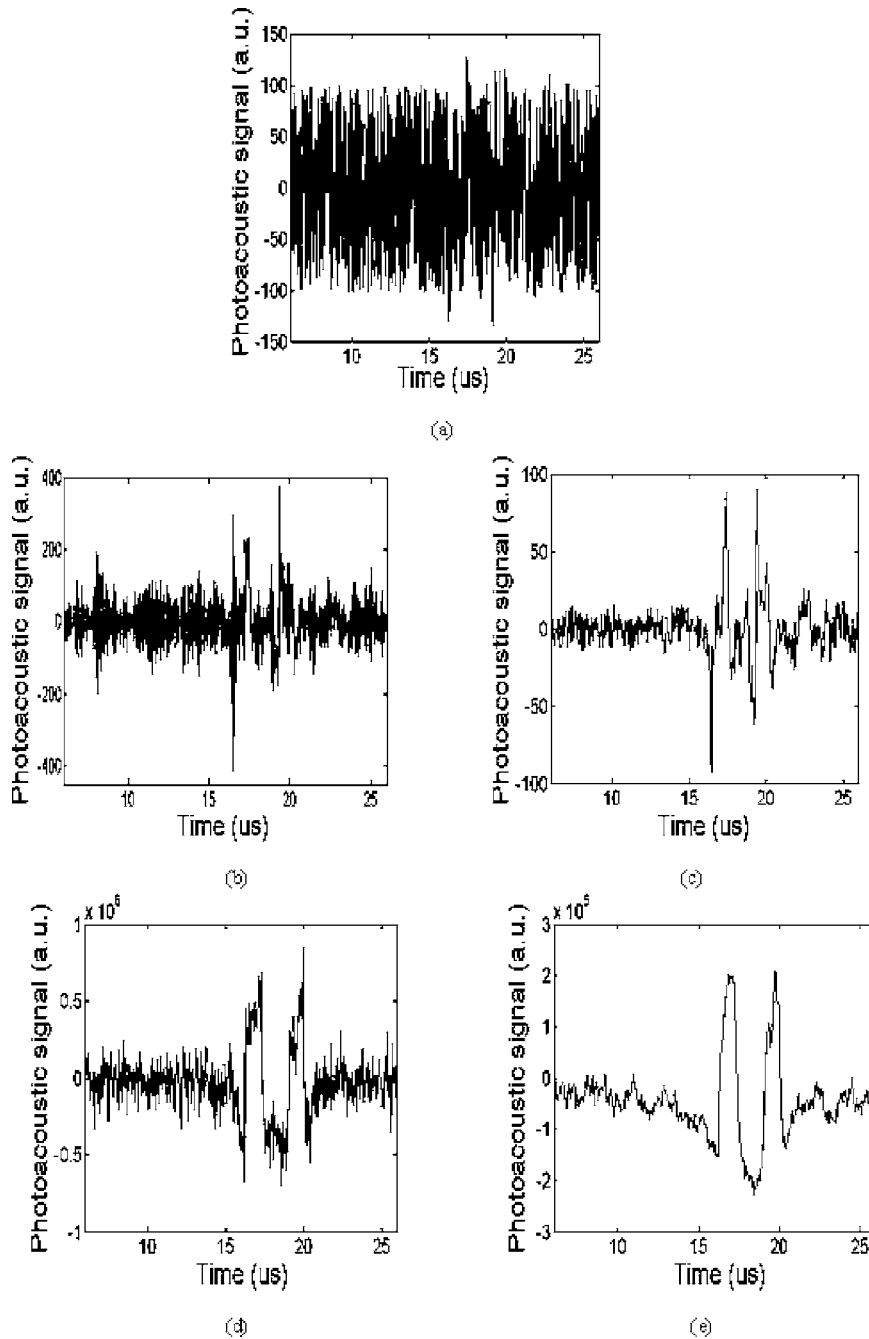
FIG. 2. Photoacoustic signal processing comparison with the two different algorithms: (a) A typical photoacoustic signal containing white noise; (b) and (c) the photoacoustic signal filtered with Hilbert filter gene and combination wavelet; (d) and (e) the reconstructed signals with Hilbert filter gene and combination wavelet after backprojection.

C. Imaging experiment

The diagnosis of early breast tumor is one of the potential application fields for PAT. The absorption coefficient between tumor tissue and normal breast tissue can be as high as 500% at the near infrared range, which is due to an increased concentration of blood and other proteins within rapidly growing tumor angiogenesis. A cylindrical turbid phantom made of a mixture (water=500 ml, gelatine=105 g, and low fat milk=100 ml) is used to simulate the optical and acoustic properties of the human breast. An annular carborubber with an outer diameter of 5.8 mm and an inner diameter of 3.1 mm is used to simulate a breast tumor with high optical

absorption and fine structure. The annular carborubber is embedded in the cylindrical breast phantom at a depth of 5 mm.

Experimental studies on animal models play essential roles in the development of preventive, diagnostic and therapeutic procedures for diseases in a wide spectrum of fields including PAT. Here, we apply PAT to noninvasively monitor *in situ* the developing blood vessels of chick embryo chorioallantoic membrane (CAM), which is used extensively as a model system for studying development,[26] cancer behavior,[27] angiogenesis,[28] and photodynamic therapy.[29] A sample of 12-day period CAM, which is covered with polyvinyl chloride film to insulate from water, was obtained from the Institute

of Animal Science Affiliated to Guangdong Academy of Agricultural Sciences.

To further explore the feasibility of deeply penetrating PAT with the modified algorithm for biological imaging, we test that on a rat brain (~300 g) with the skull and scalp intact *in vivo*. The thicknesses of the scalp and skull covering the brain are about 0.6 and 0.8 mm. Before the experiment, the rat is anesthetized by intraperitoneal injection of pentobarbital sodium (50 mg/kg animal weight), and the hair on the head of the rat is removed gently with depilatory lotion.

D. Image analysis method

Two sets of the data processing procedure by wavelet-based mFBP and FBP reconstructed algorithm are comparably analyzed in the simulated experiment. The original signal including the useful photoacoustic signal as well as strong noise data is given, and the corresponding results of signal process after filter and backprojection are analyzed, respectively. The system spatial resolution is calculated in the biological experiment on the condition that the true object has a Gaussian shape. In order to quantitatively evaluate the medical image quality of the filter results, a desired region of interest (DROI) and an undesired region of interest (UROI) are chosen from the reconstruction images, which are marked with a broken line and a real line, respectively. Two quantitative evaluation indicators of mean-to-standard-deviation ratio (MSR) and contrast-to-noise ratio (CNR) are adopted, and are calculated as $MSR = S_d/D_d$ and $CNR = |S_d - S_u|/[0.5(D_d + D_u)]^{1/2}$, Where S_d is the gray-scale mean of the DROI, D_d is the standard deviation of the DROI, S_u is the gray-scale mean of the UROI, and D_u is the standard deviation of the UROI.[30,31] The filter index of MSR shows the antinoise capability of the reconstructed algorithm, and the indicator of CNR shows the capability of improving the image contrast in the process of suppressing noise.

III. RESULTS

Figure 2(a) shows a typical photoacoustic signal which is custom added white noise with maximal amplitude of 120 MV. For comparison, the photoacoustic signals after being processed, respectively, by Hilbert filter gene with a cut-off frequency of 15 MHz and combination wavelet are shown as Figs. 2(b) and 2(c). It can be seen that the SNR of the signal based on combination wavelet improves $N_w \approx 10$ times compared with that of the original signal, and increases more than 14 dB compared with that of the Hilbert filter gene, correspondingly. The N_w is the rate of the amplitude ratio of signal to noise in Fig. 2(a) and that in Fig. 2(c). After backprojection, Figs. 2(d) and 2(e) show two typical reconstructed profile curves cutting across the central of the annular carborubber with different filter method. From the results we can see that the curve with combination wavelet is smoother, and the contrast of the peak value between the signal and background noise is sharper. A better image SNR is also obtained of the annular carborubber, whose extra- and intra-annulus are perfectly reconstructed as shown in Fig. 3(a).
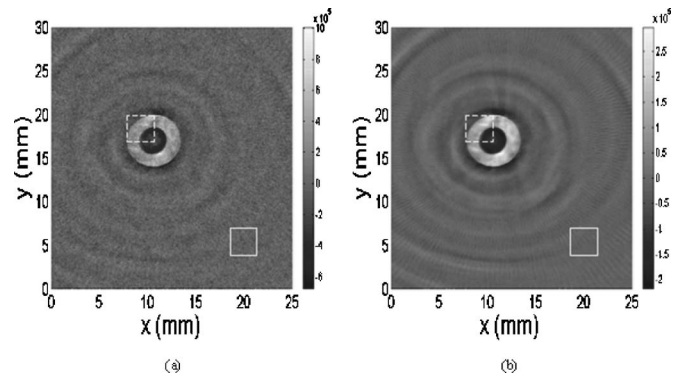

FIG. 3. PAT imaging of simulated breast tumor tissue: (a) and (b) the reconstruction PAT image by FBP algorithm with Hilbert filter and by wavelet-based mFBP algorithm.

The photoacoustic reconstruction image of the CAM *in situ* is shown in Fig. 4(b), which is in excellent agreement with the photograph of Fig. 4(a). In particular, the relative location and sizes of those blood vessels with various diameters are clearly resolved and perfectly match the original ones. Figure 5(a) shows a one-dimensional reconstructed profile including three blood vessels at position $x = 9.8$ mm of the image Fig. 4(c). Figure 5(b) gives the enlarged profile of a blood vessel (diameter ~220 μm) marked in Fig. 5(a) with spline interpolation, where the full width at half maximum value of the peak is measured at 300 μm. Generally an approximate estimate of the observed size would be the square root of the sum of the squares of the true object size
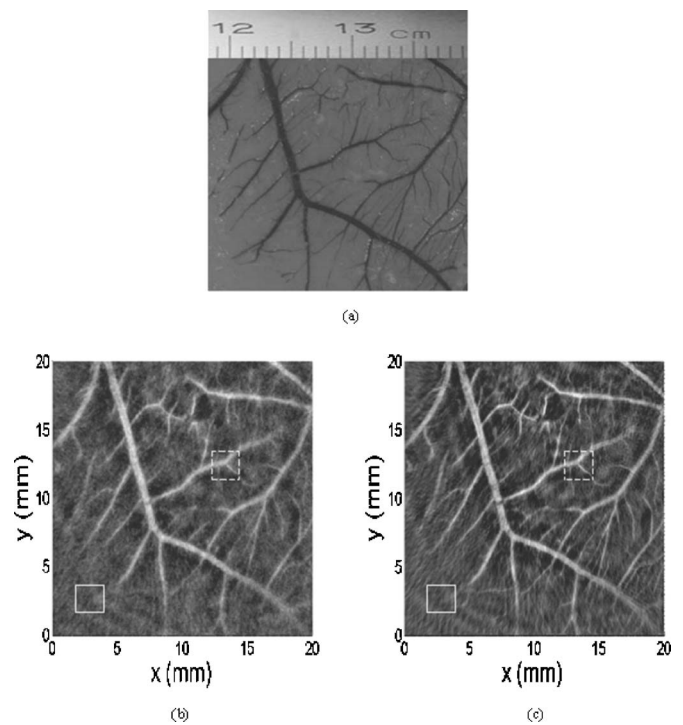

FIG. 4. PAT imaging of CAM *in situ* on the condition of strong background noise: (a) The photograph of the sample; (b) and (c) the reconstruction PAT image by FBP algorithm with RL filter and by wavelet-based mFBP algorithm.
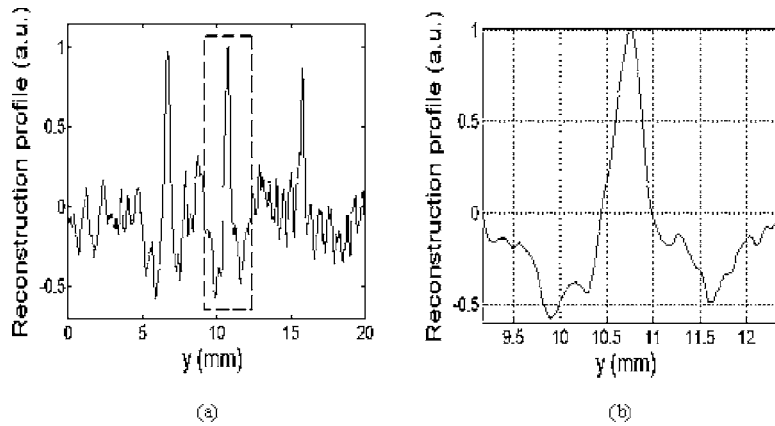
FIG. 5. One-dimensional reconstructed profile including three blood vessels at position $x=9.8$ mm of the image Fig. 4(c): (a) the reconstructed profile and (b) the enlarged profile of a blood vessel marked in Fig. 5(a).

and the spatial resolution, i.e., $300^2=220^2+r^2$, where r is the resolution. Therefore, we claim that the system spatial resolution has been improved to 204 μm.

Figure 6(a) shows the open-skull photograph acquired after the PAT experiment, and for comparison Fig. 6(b) gives a PAT image of the cortical surface of the rat brain reconstructed by standard FBP algorithm with RL filter to that reconstructed by wavelet-based mFBP algorithm. In Fig. 6(b), the major structural traits in the rat brain are blurred, and the detailed structure is covered by the noise. The image
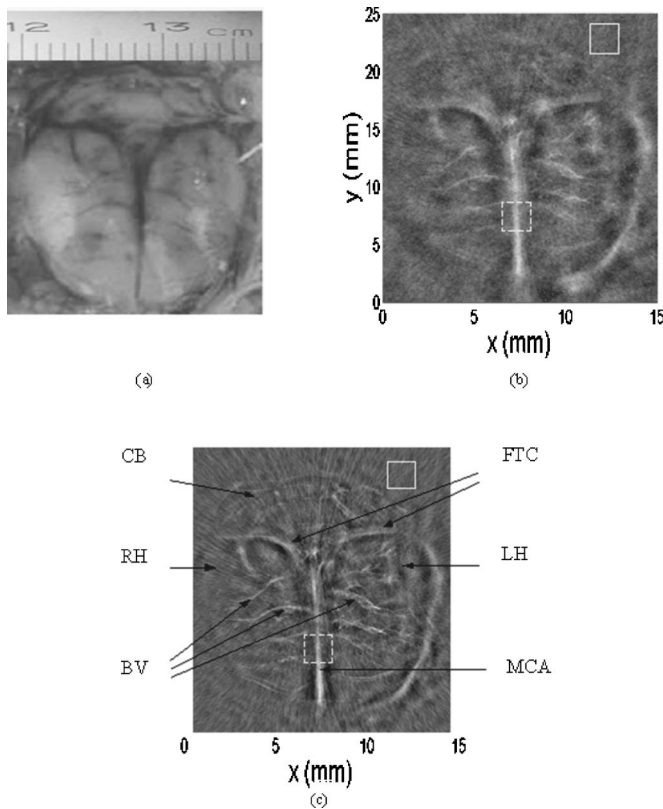

FIG. 6. PAT imaging of a rat brain *in vivo* with the skull and scalp intact: (a) Open-skull photograph of the rat brain after the PAT experiment; (b) and (c) the reconstructed PAT image of the detailed structures of the rat brain organization by FBP algorithm with RL filter and by wavelet-based mFBP algorithm: BV: blood vessel; CB: cerebellum; FTC: fissura transversa cerebri; MCA: middle cerebral artery; RH: right hemisphere; LH: left hemisphere.

SNR of Fig. 6(c) is good, and the blood vessels in the upper cerebral cortex are accurately resolved. Other detailed brain structures of the rat brain, such as the middle cerebral artery, fissura transversa cerebri and cerebellum are clearly identified in the corresponding reconstructed PAT image.

It can be seen that the wavelet-based mFBP reconstruction algorithm effectively improves the image quality compared with the FBP algorithm with RL filter, and the corresponding values of MSR and CNR are higher. In the simulating experiment, the FBP algorithm with Hilbert filter has a better capability of high-frequency recovery, because it can theoretically recover all the details with an infinite frequency bandwidth. But its capability of suppression noise is worse, and the Gibbs phenomena appearing in the filter's response may become serious. In the following biological experiments, the modified algorithm with combination wavelet obtains better image SNR and contrast, compared with that by the FBP algorithm with RL filter. Of course, with the increased detecting depth, the image quality of biological tissue would decrease because of the SNR deterioration.

IV. DISCUSSION

After a careful observation of the image, it can be found that the quality of CAM reconstructed image decreases resulting from blurring, which is caused by the following possible reasons: The tomography plane of the CAM has some drapes because of the PVC film, which may bring heterogeneous light absorption, especially on the verge of big blood vessels; The finite surface area of the detector, which has a diameter of 1 mm in this experiment, may cause blurring of the image perpendicular to the radial detection.[3] In vivo experiment, the image contrast is reduced because of the following possible reasons: (i) light attenuation further reduces the absorbed optical energy density below the cortex after the optical absorption and diffusion of the skull and scalp, (ii) the background parenchyma has an optical absorption coefficient of 0.56 cm^{-1}, (iii) the photoacoustic wave has a large attenuation and reflectibility when it travels through the parenchyma, especially through the scalp and skull.

In order to provide better resolution versus noise, the nonlinear processing to coefficients is important to keep more high-frequency details and to obtain lower noise, because the

frequency spectrum of the photoacoustic signal has a broad section from several hundreds hertz to tens of megahertz. Using wavelet thresholding technique, except for SURE approach, other threshold estimation methods may bring better filtering effect, such as minimax, CV, GCV, FDR, Bayesian approach. If considering the statistical characters of signal and noise in terms of processing coefficients, lower noise could be obtained and more high frequency could be recovered at the same time, which has been applied in medical ultrasound images.[32] Moreover, according to multiple-bandwidth photoacoustic theory,[1] the higher value of f_L and f_H could obtain better image resolution, while the major structural traits may be blurred. The smaller value of Δf could realize better frequency spectral superposition effect to suppress noise, but the computational time of the reconstructed algorithm may be longer. Those potential improvements of the mFBP algorithm to provide better resolution versus noise are our immediate future work.

The photoacoustic SNR, which is one of the most important parameters in deeply penetrating PAT, decreases exponentially with depth with a decay constant of a few millimeters.[33] The system noise mainly resulting from external disturbance of the acquisition and rotation scanning system could be decreased by electromagnetic shielding, such as electromagnetic induction resulting from laser and motor loop. But the stochastic noise could not be removed by system improvement. At present, the general method to reduce stochastic noise is multiple average signals in the procession of signal acquisition, which will prolong the data acquisition time.[4,34] The relative long time of signal acquisition hampers the practical application of photoacoustic technique, especially for *in vivo* diagnosis. In our experiments, the time of signal acquisition can be reduced by approximately 60% at the cost of increasing compute complexity for the reconstructed algorithm. The computational time to reconstruct the two-dimensional image is about 26 h using a PC with a 1.7 GHz Pentium 4 Processor. The reconstruction speed can be drastically improved with advanced computers.

In practice, in order to improve the SNR of the reconstructed image, there are several feasible methods except for a high antinoise reconstruction algorithm. First, the diagnostic window (650–900 nm) has a low absorption coefficient and a relatively low scattering coefficient in biological tissues and can, consequently, provide deep penetration for PAT imaging. For example, the laser with wavelength of 760 and 850 nm has different characteristics of absorbing two different states of the oxyhemoglobin (O_2Hb) and deoxyhemoglobin (HHb). The relative metabolic changes of O_2Hb, HHb and the total of them, the blood volume within the measured regions, can be detected for brain functional imaging.[35] Second, the photoacoustic signal strength can be enhanced by using a matched optical contrast agent. Indocyanine green, in combination with near-infrared techniques, is widely applied in angiography,[36] tumor detection,[37] and blood vessels imaging.[33] Nanoshell or nanoparticle, as a new contrast-enhancing agent, have been applied in PAT to increase optical absorption.[37,38] Third, the mechanical scanning can be replaced by electronic scanning (e.g., multi-element transducer array) to reduce the external disturbance and unreliability, which provides a near-practicality method for clinic diagnosis.[5,11,39–43]

V. CONCLUSION

This work presents an effective and efficient antinoise technique for high antinoise PAT, which is a relatively new multimodality (photo and acoustic) imaging technique. The wavelet-based mFBP algorithm shows a high capability of suppressing noise with satisfactory experiment results. A good image SNR is obtained in the simulated sample of annular carborubber, whose extra- and intra-annulus are perfectly reconstructed. Blood vessels with various diameters on the CAM *in situ* are clearly identified with a high ultrasonic resolution. Detailed tissue structures in the rat brain are also accurately mapped with less dispersion through the skull and scalp intact *in vivo*. It can be seen that the wavelet-based mFBP algorithm can provide a high-quality reconstruction image under the condition of comparable noise suppression. In the future, PAT has the potential to develop for structural and functional *in vivo* imaging of the human brain. Albeit significantly more difficult (e.g., strong background noise), is also possible with high antinoise reconstruction algorithm, near-infrared lasers, contrast-enhancing agent, multi-element transducer array, etc.

ACKNOWLEDGMENTS

a)Author to whom correspondence should be addressed; Electronic mail: xingda@scnu.edu.cn

[1] G. Ku, X. Wang, G. Stoica, and L. V. Wang, "Multiple-bandwidth photoacoustic tomography," Phys. Med. Biol. **49**, 1329–1338 (2004).

[2] J. J. Niederhauser, M. Jaeger, R. Lemor, P. Weter, and M. Frenz, "Combined ultrasound and optoacoustic system for real-time high-contrast vascular imaging *in vivo*," IEEE Trans. Med. Imaging **24**, 436–440 (2005).

[3] Y. Su, F. Zhang, K. Xu, J. Yao, and R. K. Wang, "A photoacoustic tomography system for imaging of biological tissues," J. Phys. D **38**, 2640–2644 (2005).

[4] X. Wang, Y. Pang, G. Ku, X. Xie, G. Stoica, and L. V. Wang, "Noninvasive laser-induced photoacoustic tomography for structural and functional imaging of the brain *in vivo*," Nat. Biotechnol. **21**, 803–806 (2003).

[5] D. Yang, D. Xing, H. Gu, Y. Tan, and L. Zeng, "Fast multielement phase-controlled photoacoustic imaging based on limited-field-filtered backprojection algorithm," Appl. Phys. Lett. **87**, 194101 (2005).

[6] A. A. Oraevsky, V. A. Andreev, A. A. Karabutov, D. R. Fleming, Z. Gatalica, H. Singh, and R. O. Esennaliev, "Laser opto-acoustic imaging of the breast: Detection of cancer angiogenesis," Proc. SPIE **3597**, 352–363 (1999).

[7] R. G. M. Kolkman, J. H. G. M. Klaessens, E. Hondebrink, J. C. W. Hopman, de F. F. M. Mul, W. Steenbergen, J. M. Thijssen, and van T. G. Leeuwen, "Photoacoustic determination of blood vessel diameter," Phys. Med. Biol. **49**, 4745–4756 (2004).

[8] A. A. Oraevaky, A. A. Karabutov, and S. V. Solomatin, "Laser optoacoustic imaging of breast cancer in vivo," Proc. SPIE **4256**, 352–363 (2001).

[9] C. G. A. Hoelen, de F. F. M. Mul, R. Pongers, and A. Dekker, "Three-

dimensional photoacoustic imaging of blood vessels in tissue," Opt. Lett. **23**, 648–650 (1998).

[10] M. Xu and L. V. Wang, "Pulsed-microwave-induced thermoacoustic tomography: Filtered backprojection in a circular measurement configuration," Med. Phys. **29**, 1661–1669 (2002).

[11] B. Yin, D. Xing, Y. Wang, Y. Zeng, Y. Tan, and Q. Chen, "Fast photoacoustic imaging system based on 320-element linear transducer array," Phys. Med. Biol. **49**, 1339–1346 (2004).

[12] Y. Wang, D. Xing, Y. Zeng, and Q. Chen, "Photoacoustic imaging with deconvolution algorithm," Phys. Med. Biol. **49**, 3117–3124 (2004).

[13] C. G. A. Hoelen and F. F. M. de Mul, "Image reconstruction for photoacoustic scanning of tissue structures," Appl. Opt. **39**, 5872–5883 (2000).

[14] Y. V. Zhulina, "Optimal statistical approach to optoacoustic image reconstruction," Appl. Opt. **39**, 5971–5977 (2000).

[15] R. A. Kruger, P. Liu, Y. R. Fang, and C. R. Appledorn, "Photoacoustic ultrasound (PAUS)-Reconstruction tomography," Med. Phys. **22**, 1605–1609 (1995).

[16] K. P. Kostli, M. Frenz, H. Bebie, and H. P. Weber, "Temporal backward projection of optoacoustic pressure transients using Fourier transform methods," Phys. Med. Biol. **46**, 1863–1872 (2001).

[17] M. Xu and L. V. Wang, "Time-domain reconstruction for thermoacoustic tomography in a spherical geometry," IEEE Trans. Med. Imaging **21**, 814–822 (2002).

[18] Y. Xu, D. Feng, and L. V. Wang, "Exact frequency-domain reconstruction for thermoacoustic tomography: I. Planar geometry," IEEE Trans. Med. Imaging **21**, 823–828 (2002).

[19] Y. Xu, M. Xu, and L. V. Wang, "Exact frequency-domain reconstruction for thermoacoustic tomography: II. Cylindrical geometry," IEEE Trans. Med. Imaging **21**, 829–833 (2002).

[20] M. Jansen, G. Uytterhoeven, and A. Bultheel, "Image de-noising by integer wavelet transforms and generalized cross validation," Med. Phys. **26**, 622–630 (1999).

[21] J. O. Deasy, M. V. Wickerhauser, and M. Picard, "Accelerating Monte Carlo simulations of radiation therapy dose distributions using wavelet threshold de-noising," Med. Phys. **29**, 2366–2373 (2002).

[22] O. Petrascu, A. Bel, N. Linthout, D. Verellen, G. Soete, and G. Storme, "Automatic on-line electronic portal image analysis with a wavelet-based edge detector," Med. Phys. **27**, 321–329 (2000).

[23] X. Tang, R. Ning, R. Yu, and D. Conover, "Cone beam volume CT image artifacts caused by defective cells in x-ray flat panel imagers and the artifact removal using a wavelet-analysis-based algorithm," Med. Phys. **28**, 812–825 (2001).

[24] H. Yoshida, D. D. Casalino, B. Keserci, A. Coskun, O. Ozturk, and A. Savranlar, "Wavelet-packet-based texture analysis for differentiation between benign and malignant liver tumors in ultrasound images," Phys. Med. Biol. **48**, 3735–3753 (2003).

[25] J. Gao, W. Wang, and G. Zhu, "Wavelet transform and instantaneous attributes analysis," Chin. J. Geophys. **40**, 821–832 (1997) (in Chinese).

[26] J. E. Fortune, R. A. Cushman, C. M. Wahl, and S. Kito, "The primordial to primary follicle transition," Mol. Cell Endocrinol. **163**, 53–60 (2000).

[27] A. Vacca, D. Ribatti, A. M. Roccaro, A. Frigeri, and F. Dammacco, "Bone marrow angiogenesis in patients with active multiple myeloma," Semin. Oncol. **28**, 543–550 (2001).

[28] M. Prost, "Experimental studies on the angiogenic activity of the detached retina," Graefe's Arch. Clin. Exp. Ophthalmol. **228**, 83–85 (1990).

[29] N. Lange, J. P. Ballini, G. Wagnieres, and van den H. Bergh, "A new drug-screening procedure for photosensitizing agents used in photodynamic therapy for CNV," Invest. Ophthalmol. Visual Sci. **42**, 38–46 (2001).

[30] H. Soltanian-Zadeh, J. P. Windham, and A. E. Yagle, "A multidimensional nonlinear edge-preserving filter for magnetic resonance image restoration," IEEE Trans. Image Process. **4**, 147–161 (1995).

[31] G. Cincotti, G. Loi, and M. Pappalardo, "Frequency decomposition and compounding of ultrasound medical images with wavelet packets," IEEE Trans. Med. Imaging **20**, 764–771 (2001).

[32] A. Achim, A. Bezerianos, and P. Tsakalides, "Novel Bayesian multiscale method for speckle removal in medical ultrasound images," IEEE Trans. Med. Imaging **20**, 772–783 (2001).

[33] G. Ku and L. V. Wang, "Deeply penetrating photoacoustic tomography in biological tissues enhanced with an optical contrast agent," Opt. Lett. **30**, 507–509 (2005).

[34] Y. Wang, X. Xie, X. Wang, G. Ku, K. L. Gill, D. P. O'Neal, G. Stoica, and L. V. Wang, "Photoacoustic tomography of a nanoshell contrast agent in the *in vivo* rat brain," Nano Lett. **4**, 1689–1692 (2004).

[35] J. Yang, S. Zeng, Q. Luo, L. Guan, P. Kuang, H. Gong, and B. Chance, "Left prefrontal lobe contributed to semantic encoding of unrelated word pairs: A near-infrared spectroscopy study," Acta Psychologica Sinica **33**, 48–54 (2001).

[36] B. F. Hochheimer, "Angiography of the retina with indocyanine green," Arch. Ophthalmol. (Chicago) **86**, 564–565 (1971).

[37] M. M. Haglund, M. S. Berger, and D. W. Hochman, "Enhanced optical imaging of human gliomas and tumor margins," Neurosurgery **38**, 308–317 (1996).

[38] Z. Yuan, C. Wu, H. Zhao, and H. Jiang, "Imaging of small nanoparticle-containing objects by finite-element-based photoacoustic tomography," Opt. Lett. **30**, 3054–3056 (2005).

[39] R. A. Kruger, W. L. Kiser, Jr., D. R. Reinecke, and G. A. Kruger, "Thermoacoustic computed tomography using a conventional linear transducer array," Med. Phys. **30**, 856–860 (2003).

[40] Y. Zeng, D. Xing, Y. Wang, B. Yin, and Q. Chen, "Optoacoustic and ultrasonic co-image with a linear transducer array," Opt. Lett. **29**, 1760–1762 (2004).

[41] L. Zeng, D. Xing, H. Gu, and D. Yang, "A fast microwave-induced thermoacoustic tomography system for imaging of biological tissues," Proc. SPIE **6047**, 60470k (2006).

[42] L. Zeng, D. Xing, H. Gu, D. Yang, S. Yang, and L. Xiang, "Fast microwave-induced thermoacoustic tomography based on multi-element phase-controlled focus technique," Chin. Phys. Lett. **23**, 1215–1218 (2006).

[43] D. Yang, D. Xing, Y. Tan, H. Gu, and S. Yang, "Integrative prototype B-scan photoacoustic tomography system based on a novel hybridized scanning head," Appl. Phys. Lett. **88**, 174101 (2006).